Letter Vol. 47, No. 5 / 1 March 2022 / Optics Letters 1073

Optics Letters

Optical phased array neural probes for beam-steering in brain tissue

Wesley D. Sacher,[1,2,3,*,†] Fu-Der Chen,[2,3,†] Homeira Moradi-Chameh,[4] Xinyu Liu,[1] Ilan Felts Almog,[2] Thomas Lordello,[2] Michael Chang,[4] Azadeh Naderian,[4] Trevor M. Fowler,[1] Eran Segev,[1] Tianyuan Xue,[2] Sara Mahallati,[4] Taufik A. Valiante,[4,5,6] Laurent C. Moreaux,[1] Joyce K. S. Poon,[2,3] and Michael L. Roukes[1]

[1]Division of Physics, Mathematics, and Astronomy, California Institute of Technology, Pasadena, California 91125, USA
[2]Department of Electrical and Computer Engineering, University of Toronto, 10 King's College Rd., Toronto, Ontario M5S 3G4, Canada
[3]Max Planck Institute of Microstructure Physics, Weinberg 2, 06120, Halle, Germany
[4]Krembil Research Institute, Division of Clinical and Computational Neuroscience, University Health Network, Toronto, Ontario, Canada
[5]Division of Neurosurgery, Department of Surgery, Toronto Western Hospital, University of Toronto, Toronto, Ontario, Canada
[6]Institute of Biomaterials and Biomedical Engineering, University of Toronto, Toronto, Ontario, Canada
*Corresponding author: wesley.sacher@mpi-halle.mpg.de
†These authors contributed equally to this work.

Received 26 August 2021; revised 28 November 2021; accepted 9 December 2021; posted 13 December 2021; published 18 February 2022

Implantable silicon neural probes with integrated nanophotonic waveguides can deliver patterned dynamic illumination into brain tissue at depth. Here, we introduce neural probes with integrated optical phased arrays and demonstrate optical beam steering *in vitro*. Beam formation in brain tissue is simulated and characterized. The probes are used for optogenetic stimulation and calcium imaging.

https://doi.org/10.1364/OL.441609

Genetically encoded optogenetic actuators and fluorescence indicators are powerful tools in the interrogation of brain activity, enabling the control and imaging of neurons with high cell-type specificity and single-cell spatial resolution [1–3]. Today's optogenetics and functional fluorescence imaging experiments often use multiphoton microscopes and implantable fiber optics, which are typically built from bulk components and are physically large and complex [4]. Yet, silicon (Si) integrated photonics have led to the dense integration of nanoscale waveguides and devices into complex, millimeter-scale circuits [5,6]. Thus, Si photonic technology can be leveraged to create nanophotonic tools that miniaturize systems for delivering light into brain tissues in ways beyond bulk optics. An approach is an implantable photonic chip that generates patterned illumination in brain tissues at depths inaccessible by free-space optics, i.e., beyond the optical attenuation length. Along these lines, nanophotonic waveguides with grating light emitters [7–10] and micro-light-emitting diodes (μLEDs) [11] have been integrated onto implantable Si probes. In brain tissues, because light mostly scatters forward [12], low-divergence beams can be emitted from gratings over distances of 200–300 μm [7,8]. Compared to μLEDs, nanophotonic waveguide-based probes do not generate excess heat beyond that caused by the light itself, can more precisely tailor the optical emission profile, are compatible with commercial wafer-scale foundry manufacturing [9,13], and can achieve a high light source density. Furthermore, as evidenced by the recent advancements in on-chip photonic beam-forming [5,14–17], sophisticated photonic circuits can enable precisely patterned illumination with high spatial resolution.

Here, we report the first implantable Si neural probes capable of optical beam-steering in tissue. The probes use silicon nitride (SiN) optical phased arrays (OPAs) as light emitters; the emitted beams are steered by wavelength tuning. The OPAs are designed to operate at blue wavelengths for the excitation of the opsin channelrhodopsin-2 (ChR2) and the genetically encoded calcium indicator GCaMP6. The probes are validated *in vitro* in mouse brain slices, demonstrating sufficient power for optogenetic stimulation and functional imaging as well as spatial control of the beam on the neuron scale. A preliminary report of this work appeared in [18].

Figure 1 shows the OPA neural probes, which consisted of 4 shanks, each ~ 18 μm thick, 3 mm long, and 50 μm wide, on a 250 μm pitch, and a thicker base region. The SiN waveguides were 200 nm thick. The probes were fabricated on 100 mm diameter silicon-on-insulator wafers as in [7]. Each shank had 4 OPAs, as shown in Fig. 1(b). A star coupler split the light in the input waveguide into 16 delay lines, and each terminated with a light-emitting grating. As the input wavelength was tuned, the differential phase-shift between the gratings led to one-dimensional angular steering of the emission [19]; the position of the OPAs on the probe was a second degree of freedom for the emission pattern. The delay lines consisted of waveguides with an initial single-mode width of 240 nm following the star coupler for a length of 12 μm that adiabatically widened to 400 nm to reduce phase error. The differential length of the delay lines was 16 μm, chosen so the free spectral range (~ 6 nm) matched the wavelength tuning range of our external cavity diode laser of 484.3 to 491 nm. The pitch and width of the

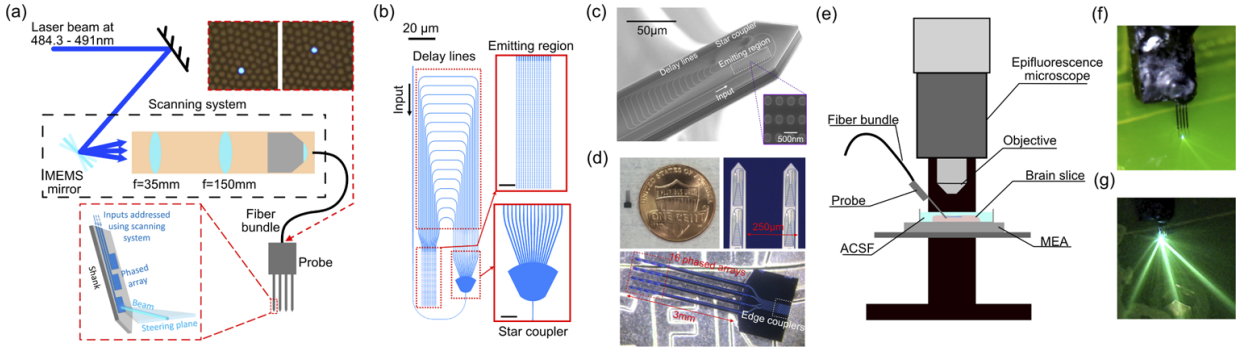

Fig. 1. OPA neural probes. (a) Schematic of the OPA neural probe connected to the scanning system. (inset) Optical micrographs of an image fiber bundle facet with cores addressed by the scanning system. (b) Schematic of the OPA design; inset scale bars are 5 μm. (c) Scanning electron micrograph (SEM) of one probe shank. (inset) SEM of a portion of the SiN gratings prior to top cladding deposition. (d) Photograph and micrographs of an OPA neural probe. (e) Illustration of the setup for testing the neural probes in brain slices. Abbreviations: MEA, microelectrode array; ACSF, artificial cerebrospinal fluid. (f), (g) Photographs of the packaged OPA neural probe emitting light in fluorescein; panel (f) has a smaller field of view and external illumination applied for visibility of the shanks, panel (g) shows the emitted beams (zoomed out, no illumination). Panels (c), (d),(f),(g) are from [18]; the fiber bundle inset of panel (a) is from [9].

arrayed gratings in the OPA were 700 nm and 300 nm, respectively. The period of each grating was 440 nm; in water, the steering plane [Fig. 1(a)] was at ~ 25° from the normal of the probe. The OPAs were designed for low crosstalk between the arrayed waveguides. The array pitch was larger than the half-wavelength criterion for emission of a single grating order, and typically three lobes were emitted from each OPA. Optimization of the array pitch, increased SiN thickness for higher optical confinement and lower crosstalk, and apodization [15] may suppress these additional lobes. In the following, we focus on one neural probe that was packaged and studied in detail.

The probe was passive to reduce tissue heating, and the 16 OPAs on the probe were independently addressed spatially using the scheme in [9,20]. As shown in Fig. 1(a), a microelectromechanical system (MEMS) mirror deflected a laser beam into cores of an image fiber bundle attached to the probe base. Each fiber core was aligned to an edge coupler on the probe, which was connected to an OPA on the shank. The switching time of the MEMS mirror was ~ 5 ms. The maximum optical power emitted by an OPA was ~ 5–10 μW and was used for Figs. 2–4.

To characterize the emitted beam profiles in non-scattering media, the probe was immersed in a fluorescein solution to image the fluorescence [9]. The setup in Fig. 1(e) was used, but with the chamber replaced with a container of fluorescein; the probe was angled so the emitted beams were parallel to the fluid surface. Top-down images of the emission pattern from the probe at a few wavelengths are shown in Fig. 2(a). Tuning the wavelength from 484.3 to 491 nm, the beams were steered continuously ±16° with narrow (neuron-scale) beams formed within a distance of 300 μm (Fig. 2); continuous steering is shown in Visualization 1. The two side lobes were at angles of about ±32° from the main beam. Figure 2(b) shows the beam profile imaged from the side; the full width at half maximum (FWHM) thickness was <19 μm over a 300 μm propagation distance. The peak intensity of the main lobe was 7× to 17× larger than the background light intensity at propagation distances of 50 to 300 μm, Fig. 2(a). A significant part of the background arose from optical scattering from the photonic circuit.

OPA beam formation in brain tissue was verified and investigated in simulation and experiment. The simulation is described in Supplement 1; the scattering coefficient (μ_s) = 200 cm^{-1}, absorption coefficient (μ_a) = 0.62 cm^{-1}, and tissue anisotropy (g) = 0.83. The simulated beam profiles, Fig. 3(a), show that the optical scattering leads to broadening of the emitted beams, a background generated between the lobes, and a reduction in intensity with propagation distance. Over the majority of the steering range, the FWHM beam width is <17 μm and the ratio of peak beam intensity to background intensity is >2.8 for propagation distances of 50 to 150 μm, Figs. 3(c), 3(d), S1, and S2. Experimental validation of the OPAs in brain tissue was performed by inserting the probe at shallow depths (OPA <100 μm from the surface) into perfused *in vitro* brain slices from adult transgenic mice

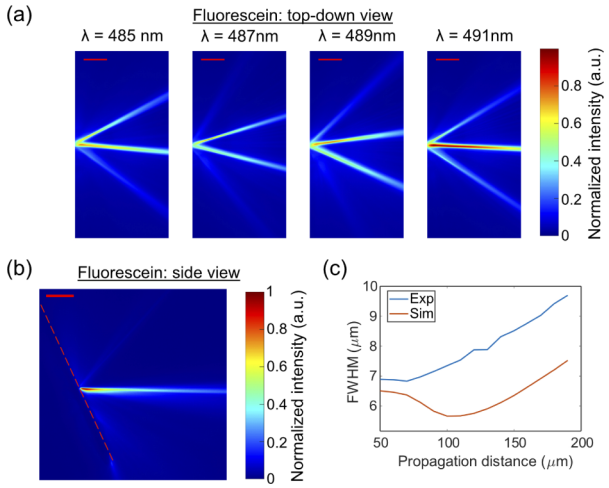

Fig. 2. Characterization of the neural probe beam profiles in fluorescein. (a) Top-down beam profiles at various wavelengths (λ). (b) Side beam profile at λ = 484.3 nm; the surface of the shanks is delineated by the dashed line. The scale bars are (a) 50 μm, (b) 100 μm. (c) Top-down measured (Exp, upper curve) and simulated (Sim, in water, lower curve) FWHM beam width versus propagation distance of the central lobe at λ = 491 nm.

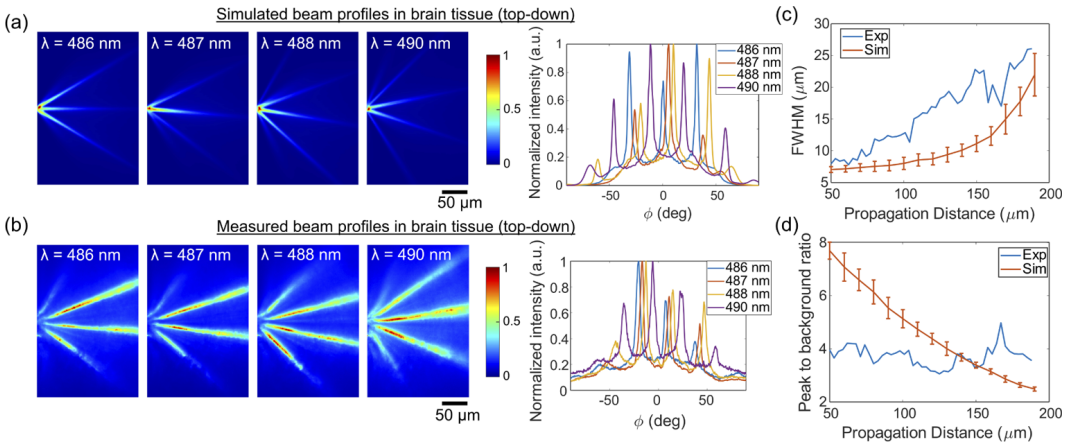

Fig. 3. OPA intensity profiles in brain tissue. (a) Top-down view of the simulated (from one calculation) and (b) measured beam profiles at four wavelengths. In panel (b), the probe was inserted into a brain slice from a VGAT-ChR2-EYFP mouse [see Fig. 1(e)]. Left, top-down intensity beam profiles; right, intensity versus emission angle (ϕ) at a propagation distance of 100 μm (i.e., along arcs of radius 100 μm centered on the emitting region of the OPA). Measured and simulated (c) FWHM beam width (Exp, upper curve; Sim, lower curve), and (d) ratios of peak beam intensity to background intensity vs. propagation distance for λ = 490 nm (Exp, lower curve; Sim, upper curve). "Sim" has been averaged over 10 simulations with different phase masks (see Supplement 1) and the bars represent the standard deviation.

co-expressing ChR2 and yellow fluorescent protein (VGAT-ChR2-EYFP, [21]) and another strain of mice expressing the calcium indicator GCaMP6s (Thy1-GCaMP6s, [2]). The tissue preparation is described in Supplement 1. All experimental procedures described here were reviewed and approved by the animal care committees of the University Health Network in accordance with the guidelines of the Canadian Council on Animal Care.

Fluorescence images of the OPA beam profiles in cerebellar brain slices from the VGAT-ChR2-EYFP mice were captured using the excitation of the YFP by the OPA illumination and the setup in Fig. 1(e). Steerable beams were formed [Figs. 3(b)–3(d) and S2] with the FWHM beam width <23 μm and the ratio of peak beam intensity to background intensity >2.7 for propagation distances of 50 to 150 μm. Continuous beam steering in brain slices is shown in Visualization 2 and Visualization 3 in the supplementary material. The main lobe had five resolvable spots at 100 μm of propagation distance (compared with seven in fluorescein). Cerebellar slices were selected for their relatively uniform YFP labeling; some non-uniformity was evident

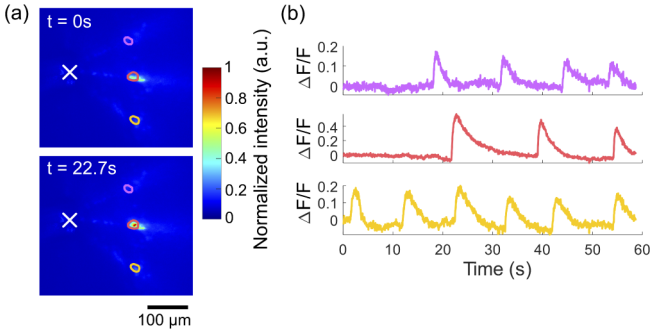

Fig. 4. Functional imaging using the OPA neural probe in a brain slice from a Thy1-GCaMP6s mouse. (a) Top-down fluorescence images at t = 0 s and 22.7 s showing a calcium event in the central lobe (OPA emitter position marked with "X." (b) Fluorescence change ($\Delta F/F$) traces of the regions delineated in (a).

from the intensity maxima in the top-down images of Fig. 3(b). The simulations and measurements differ the most near the OPA; potential causes include tissue damage near the shank, YFP bleaching (owing to the high intensity near the shank), spatial variations in YFP concentration (owing to labeling non-uniformity and the spatial distribution of labeled cells), and possible differences in scattering properties between the cortex (used for simulations) and the cerebellum. As a test of functional imaging, the probe was inserted into a region near the hippocampus in a brain slice from a Thy1-GCaMP6s mouse. The imaging apparatus are described in Supplement 1, Section 2. The lobes of the OPA illuminated three neurons, or small clusters thereof, and spontaneous time-dependent fluorescence was detected with high contrast, Fig. 4. The half rise/decay times of the calcium events (0.34 s/1.35 s on average, respectively) agreed with reported GCaMP6s dynamics for bursts of spikes [2].

Optogenetic stimulation was tested by inserting the probe into VGAT-ChR2-EYFP mouse cerebellar slices. Here, the probe orientation was modified so that the light was emitted nearly orthogonal to the tissue surface [Fig. 5(a)]. Pulsed light was applied, and extracellular electrophysiological signals were recorded by a microelectrode array (MEA) under the brain slice (stimulation details in Supplement 1, Section 4). The MEA electrodes were 30 μm in diameter arranged in a square grid with a 100 μm pitch. Robust spiking with illumination from the neural probe was observed [Figs. 5(c) and S3 (Supplement 1)], showing that the optical intensity was sufficient for optogenetic stimulation. However, the precise positions of the stimulated neurons relative to the OPA and electrodes were unknown. Spatial differences in the activity patterns across the MEA were not repeatable with the steering of the beam. We hypothesize this arose from one or more of the following reasons: (1) the interconnectedness of the neurons; (2) ChR2 expression in inhibitory rather than excitatory cells in VGAT-ChR2-EYFP mice; and (3) the spacing between the OPA lobes and background between them. Figure 5(e) and the analysis in Supplement 1 (Section 6 and Fig. S5) support the first two hypotheses. Figure 5(e) shows

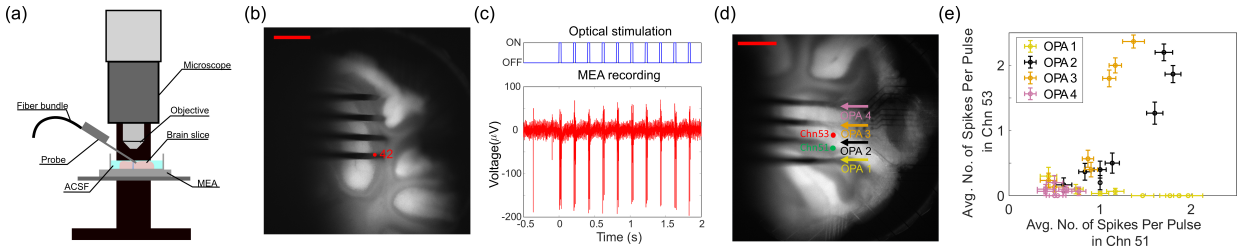

Fig. 5. Optogenetic stimulation by the neural probe (fixed wavelength) in VGAT-ChR2-EYFP mouse cerebellar slices on an MEA. (a) Diagram of the setup. (b) Fluorescence image of the brain slice with the probe. Channel ("Chn") 42 of the MEA is marked. The scale bar is 500 μm. (c) Recording on MEA Chn 42 under illumination from the nearest OPA. (d) Fluorescence image of another brain slice with the probe. MEA Chn 53 and 51, and the positions of four OPAs are marked. The scale bar is 500 μm. (e) Average number of spikes per optical pulse on MEA Chn 53 and 51 with optical stimulation from the OPAs in panel (d). The spikes were sorted, and both channels recorded one single unit for this experiment. Each point is from a stimulation trial of three sets of ten optical pulses (pulse width, 50 ms; period, 200 ms; recovery period between each set of pulses, 10 s). For each OPA, the optical power was reduced across the trials. The error bars show the standard error of the mean spikes per pulse during a trial.

the correlation in the spiking activity recorded at two microelectrodes in the same MEA column (Channels 53 and 51) arising from excitation from four OPAs on the probe. Here, illumination from one OPA on each shank was sequentially applied (the OPAs belong to the same row), and trials with decreasing optical power were performed. Generally, the number of spikes per pulse increased with the optical power (Fig. S4). The spike rates on Channels 53 and 51 indicated that lateral shifts of the illumination of the order of the shank pitch (250 μm > steering of OPA beams) were necessary for repeatable changes in the activity patterns on the MEA (e.g., comparing the trends of OPAs 1 and 2), phenomenologically similar to observations in [11].

In sum, we have presented the first implantable Si neural probes with integrated OPAs for generating steerable optical beams in brain tissue for optogenetic stimulation and functional imaging. Future experiments in the stimulation of individual neurons may benefit from simultaneous functional imaging to identify the stimulated neurons. OPAs at green/red wavelengths can be realized with larger feature sizes for excitation of other opsins and fluorophores. These results show the possibilities for delivering dynamically patterned illumination at depth in brain tissues for brain activity mapping [22].

Funding. National Institutes of Health (NS090596, NS099726); Caltech Kavli Nanoscience Institute; Canadian Institutes of Health Research; Natural Sciences and Engineering Research Council of Canada.

Disclosures. The authors declare no conflicts of interest.

Data availability. Data underlying the results presented in this Letter are not publicly available at this time but may be obtained from the authors upon reasonable request.

Supplemental document. See Supplement 1 for supporting content.

REFERENCES

1. K. Deisseroth, Nat. Neurosci. **18**, 1213 (2015).
2. H. Dana, T.-W. Chen, A. Hu, B. C. Shields, C. Guo, L. L. Looger, D. S. Kim, and K. Svoboda, PLoS One **9**, e108697 (2014).
3. V. Villette, M. Chavarha, I. K. Dimov, J. Bradley, L. Pradhan, B. Mathieu, S. W. Evans, S. Chamberland, D. Shi, R. Yang, B. B. Kim, A. Ayon, A. Jalil, F. St-Pierre, M. J. Schnitzer, G. Bi, K. Toth, J. Ding, S. Dieudonné, and M. Z. Lin, Cell **179**, 1590 (2019).
4. A. M. Packer, L. E. Russell, H. W. P. Dalgleish, and M. Häusser, Nat. Methods **12**, 140 (2015).
5. J. Sun, E. Timurdogan, A. Yaacobi, E. S. Hosseini, and M. R. Watts, Nature **493**, 195 (2013).
6. C. R. Doerr, Front. Phys. **3**, 37 (2015).
7. E. Segev, J. Reimer, L. C. Moreaux, T. M. Fowler, D. Chi, W. D. Sacher, M. Lo, K. Deisseroth, A. S. Tolias, A. Faraon, and M. L. Roukes, Neurophotonics **4**, 011002 (2016).
8. S. Libbrecht, L. Hoffman, M. Welkenhuysen, C. Van den Haute, V. Baekelandt, D. Braeken, and S. Haesler, J. Neurophysiol. **120**, 149 (2018).
9. W. D. Sacher, F.-D. Chen, H. Moradi-Chameh, X. Luo, A. Fomenko, P. Shah, T. Lordello, X. Liu, I. Felts Almog, J. N. Straguzzi, T. M. Fowler, Y. Jung, T. Hu, J. Jeong, A. M. Lozano, P. G.-Q. Lo, T. A. Valiante, L. C. Moreaux, J. K. S. Poon, and M. L. Roukes, Neurophotonics **8**, 025003 (2021).
10. A. Mohanty, Q. Li, M. A. Tadayon, S. P. Roberts, G. R. Bhatt, E. Shim, X. Ji, J. Cardenas, S. A. Miller, A. Kepecs, and M. Lipson, Nat. Biomed. Eng. **4**, 223 (2020).
11. F. Wu, E. Stark, P.-C. Ku, K. D. Wise, G. Buzsáki, and E. Yoon, Neuron **88**, 1136 (2015).
12. G. Yona, N. Meitav, I. Kahn, and S. Shoham, eNeuro **3**, ENEURO.0059-15.2015 (2016).
13. W. D. Sacher, X. Luo, Y. Yang, F.-D. Chen, T. Lordello, J. C. C. Mak, X. Liu, T. Hu, T. Xue, P. G.-Q. Lo, M. L. Roukes, and J. K. S. Poon, Opt. Express **27**, 37400 (2019).
14. C. V. Poulton, M. J. Byrd, M. Raval, Z. Su, N. Li, E. Timurdogan, D. Coolbaugh, D. Vermeulen, and M. R. Watts, Opt. Lett. **42**, 21 (2017).
15. D. N. Hutchison, J. Sun, J. K. Doylend, R. Kumar, J. Heck, W. Kim, C. T. Phare, A. Feshali, and H. Rong, Optica **3**, 887 (2016).
16. D. Kwong, A. Hosseini, J. Covey, Y. Zhang, X. Xu, H. Subbaraman, and R. T. Chen, Opt. Lett. **39**, 941 (2014).
17. J. Midkiff, K. M. Yoo, J. D. Shin, H. Dalir, M. Teimourpour, and R. T. Chen, Optica **7**, 1544 (2020).
18. W. D. Sacher, X. Liu, F.-D. Chen, H. Moradi-Chameh, I. F. Almog, T. Lordello, M. Chang, A. Naderian, T. M. Fowler, E. Segev, T. Xue, S. Mahallati, T. A. Valiante, L. C. Moreaux, J. K. S. Poon, and M. L. Roukes, in Conference on Lasers and Electro-Optics (Optical Society of America, 2019), p. ATh4I.4.
19. K. Van Acoleyen, W. Bogaerts, and R. Baets, IEEE Photonics Technol. Lett. **23**, 1270 (2011).
20. A. N. Zorzos, J. Scholvin, E. S. Boyden, and C. G. Fonstad, Opt. Lett. **37**, 4841 (2012).
21. S. Zhao, J. T. Ting, H. E. Atallah, L. Qiu, J. Tan, B. Gloss, G. J. Augustine, K. Deisseroth, M. Luo, A. M. Graybiel, and G. Feng, Nat. Methods **8**, 745 (2011).
22. L. C. Moreaux, D. Yatsenko, W. D. Sacher, J. Choi, C. Lee, N. J. Kubat, R. J. Cotton, E. S. Boyden, M. Z. Lin, L. Tian, A. S. Tolias, J. K. Poon, K. L. Shepard, and M. L. Roukes, Neuron **108**, 66 (2020).